Understanding the Optoelectronic Processes in Colloidal 2D Multi-Layered MAPbBr$_3$ Perovskite Nanosheets: Funneling, Recombination and Self-Trapped Excitons

André Niebur, Eugen Klein, Rostyslav Lesyuk, Christian Klinke, and Jannika Lauth*

Colloidal chemistry methods have made quasi 2D perovskites readily accessible. Ultrathin perovskites exhibit charge transport properties which are beneficial for solar cells and the combination of layers with different thicknesses directs charge carriers toward thicker layers with a smaller bandgap. However, detailed knowledge about the mechanisms by which excitons and charge carriers funnel and recombine in these structures is lacking. Here, colloidal 2D methylammonium lead bromide (MAPbBr$_3$) Ruddlesden-Popper perovskites with a broad combination of layers ($n = 3$ to 10, and bulk fractions with $n > 10$) is characterized by femtosecond transient absorption spectroscopy and time-resolved photoluminescence. It is found that second- and third-order processes dominate in MAPbBr$_3$ nanosheets, indicating exciton-exciton annihilation (EEA) and Auger recombination. Long-lived excitons in thin layers (e.g., $n = 5$, $E_b = 136$ meV) funnel into high n within 10–50 ps, which decreases their exciton binding energy below $k_B T$ and leads to radiative recombination. Parallel and consecutive funneling compete with trapping processes, making funneling an excellent tool to overcome exciton self-trapping when high-quality n-n interfaces are present. Free charge carriers in high-n regions on the other hand facilitate radiative recombination and EEA is bypassed, which is desirable for LED and lasing applications.

1. Introduction

The energy of sunlight reaching Earth could cover the global energy consumption more than 8000-fold.[1] We therefore need to make this abundant energy source more accessible through affordable solar cells. Such devices based on cost efficient perovskites exhibit steadily increasing efficiencies exceeding 26% (or 33% in tandem solar cells with Si).[2] Besides, perovskites are appealing for many optoelectronic applications, since they show a tunable bandgap,[3,4] near unity photoluminescence quantum yield (PLQY),[5] and sharp emission.[6] In this context, the underlying photophysics in colloidal 2D methylammonium lead bromide (MAPbBr$_3$) nanosheets, especially on an ultrafast timescale, is crucial for energy conversion.

Metal halide perovskites have the formula ABX$_3$, where A is a small cation, most prominently methylammonium (MA, CH$_3$NH$_3^+$) or Cs$^+$, B is a metal, and X is a halogen, forming a corner-connected

A. Niebur, J. Lauth
Institute of Physical Chemistry and Electrochemistry
Leibniz University Hannover
Callinstr. 3a, D-30167 Hannover, Germany
E-mail: jannika.lauth@uni-tuebingen.de

A. Niebur, J. Lauth
Cluster of Excellence PhoenixD (Photonics Optics
and Engineering – Innovation Across Disciplines)
D-30167 Hannover, Germany

E. Klein, R. Lesyuk, C. Klinke
Institute of Physics
University of Rostock
Albert-Einstein-Straße 23, 18059 Rostock, Germany

R. Lesyuk
Pidstryhach Institute for Applied Problems of Mechanics and
Mathematics of NAS of Ukraine
Naukowa Str. 3b, Lviv 79060, Ukraine

C. Klinke
Department Life
Light & Matter
University of Rostock
Albert-Einstein-Strasse 25, 18059 Rostock, Germany

C. Klinke
Department of Chemistry
Swansea University – Singleton Park
Swansea SA2 8PP, UK

J. Lauth
Laboratory of Nano and Quantum Engineering (LNQE)
Leibniz University Hannover
Schneiderberg 39, D-30167 Hannover, Germany

J. Lauth
Institute of Physical and Theoretical Chemistry
University of Tübingen
Auf der Morgenstelle 18, D-72076 Tübingen, Germany

$[BX_6]^{4-}$ octahedron. The small cations are located in the gaps of the B–X structure. When introducing a large organic cation A′, metal halide perovskites can form layered structures with a $A'_2A_{n-1}B_nX_{3n+1}$ stoichiometry known as quasi-2D Ruddlesden–Popper perovskites (RPP) with n being the number of octahedron layers, becoming less rigid for smaller n.[7] The thinnest RPP ($n = 1$) is a single layer of B–X octahedrons, which is stabilized by the large organic cations on both sides. The research focused on controlling the number of B–X octahedron layers n is receiving increasing interest since controlling n allows additional tailoring of optoelectronic properties into the direction of the design of complex band alignments.[8] Among others, studies on the (octahedral) layer numbers have been published for perovskites of the types $MAPbI_3$,[4,9–11] $MAPbBr_3$,[4,12,13] $MAPbCl_3$,[4] $CsPbBr_3$[14,15] and lead free alternatives including $MASnI_3$, $MAGeI_3$, and $CsSnI_3$.[16,17] This series of materials covers the full visible spectrum from the UV ($MAPbCl_3$) to the NIR ($MAPbI_3$) and the structures have proven to be efficient absorbers and emitters for solar cells and in LEDs.[18,19] Tin-based perovskites offer a highly efficient lead-free material platform for applications, however, they also suffer from a rather high degradation.[20,21]
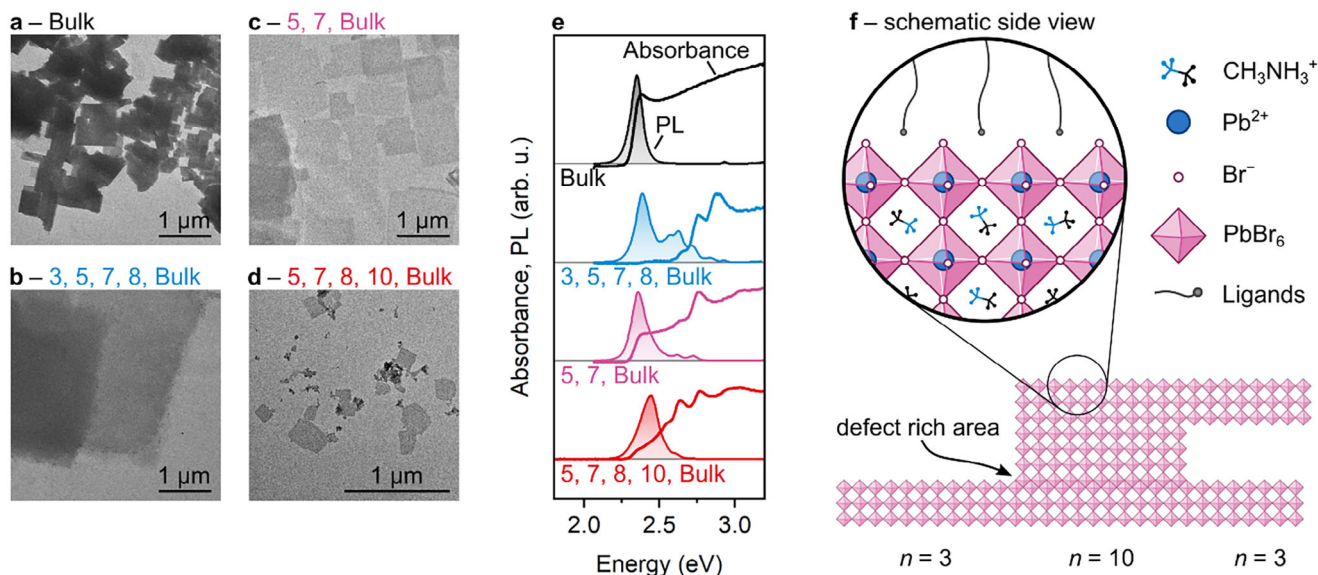
By reducing the layers of 2D metal halide perovskites to a single-digit number of crystal units, an atomically precise confinement is introduced, which leads to optoelectronic properties being mainly dependent on the material thickness with lateral sizes often playing a minor role. Furthermore, the properties of these ultrathin perovskites reflect the interplay between quantum confinement and dielectric confinement. The latter reduces Coulomb screening of excitons in nanosheets with a reduced thickness due to a dielectric mismatch with the surrounding medium and effectively increases the exciton binding energy.[22,23] Blancon et al. have shown for $MAPbI_3$ RPPs that with reduced thickness, the bandgap, exciton binding energy, and the effective mass of the excitons increase. They attribute this behavior to band mixing and non-parabolic effects.[24] Milot et al. reported a 25-fold lower carrier mobility with decreasing n in $MAPbI_3$ RPPs, which they associated with a higher exciton binding energy caused by stronger charge carrier confinement.[25] In the context of solar cells, an appealing strategy is to combine different perovskite layer thicknesses to exploit smaller exciton binding energies in high-n RPPs with the directional carrier motion due to band alignment. The detailed charge carrier dynamics of mixed- and multi-n RPPs provide information on ways to refine these structures. For example it has been demonstrated, that excitons in $CsPbBr_3$ RPPs can be trapped by uncoordinated Pb^{2+} on the way to high-n regions, which is suppressed by methanesulfonate treatment.[15] Besides, it is crucial whether the crystal contact between different layers is epitaxial. According to Li et al., the n-n interface determines how quickly charge carriers are funneled into high-n regions, which was shown for a $MAPbI_3$ RPP with $n = 3, 4, 5$, and bulk.[9] The authors found that electrons funnel with $\tau < 500$ fs into the bulk if the n-n contact is epitaxial, whereas $\tau > 290$ ps is described for a highly defective interface. Recently, Oddo et al. showed evidence for the funneling of energy rather than charge carriers in mixed-n $CsPbBr_3$ RPPs, which they supported with femtosecond transient absorption spectroscopy (TAS).[26]

Here, we focus on studying Auger and funneling processes in colloidal 2D multi-layered $MAPbBr_3$ RPPs, since non-radiative Auger recombination limits the efficiency in nanocrystal LEDs and shortens the lifetime of gain, therefore preventing efficient stimulated emission and lasing.[27–29] We apply steady-state absorption, TAS, PL, and time-resolved PL (time-correlated single photon counting, TCSPC) and support our findings with material characterizing methods including TEM and XRD. The 2D multi-n perovskites investigated here are synthesized based on a previously published method by Klein et al. and exhibit a layer thickness of $n = 3, 5, 7, 8, 10$, and bulk ($n > 10$) which are stacked in different thickness combinations. This means that individual 2D perovskite nanosheets contain layers of multiple thicknesses at the same time.[4] The mixed-n structure potentially solves the challenge of exciton-exciton annihilation, occurring at high excitation fluences. We apply Elliott theory for steady-state absorption[30] and an extended time-resolved Elliott model for the exited state absorption[31] to determine the transient number of excited charge carriers N_e. We find that N_e decays with mixed second- and third-order kinetics, which is indicative of bi-molecular radiative recombination, exciton-exciton annihilation (EEA), and a three-body Auger process. Most importantly we show that funneling is neither strictly parallel nor consecutive and carriers can accumulate in bulk-like or intermediate regions, from where they recombine radiatively. With increased photoexcitation fluences, we find evidence for self-trapping of excitons which in turn start to compete with the funneling. Our results not only illustrate which different ultrafast processes can occur in colloidal multi-n $MAPbBr_3$ RPPs, but also help to understand and describe how funneling can be used for, e.g., directed energy transfer, which is important for highly efficient solar cells and LEDs.

2. Results and Discussion

2.1. Structural Characterization of Multi-Layered $MAPbBr_3$

2D $MAPbBr_3$ perovskites were synthesized by first preparing $PbBr_2$ nanosheets, which were converted into $MAPbBr_3$ by a reaction with methylammonium bromide.[4] The conversion was performed at 160 °C in diphenyl ether and a mixture of dodecylamine and trioctylphosphine as ligands. Targeted layer numbers (3, 5, 7, 8, 10, and bulk) were obtained by using oleylamine instead of dodecylamine, and by varying the reaction temperature, time, and concentration of precursors[4] (see SI for detailed syntheses). **Figure 1a–d** shows TEM images of predominantly rectangular $MAPbBr_3$ perovskite nanosheets with lateral sizes between 50 nm and 5 μm. The layer numbers were validated by UV/vis and PL spectroscopy, showing distinct features which are assigned to the respective n, in accordance with the literature.[4,32,33] The sample containing $n = 5, 7, 8, 10$, and bulk (Figure 1d) is shown in twice the magnification with respect to the others due to its smaller size (a TEM cutout of the same size as for the other samples is shown in Figure S1, Supporting Information). Figure 1e shows multi-layered $MAPbBr_3$ nanosheet UV/Vis and PL spectra. The mixtures, e.g., the sample containing 5, 7 layers and a bulk fraction, has one distinct absorbance maximum and two shoulders at 2.76, 2.64, and 2.38 eV, resp., with

2402923 (2 of 11)

**ADVANCED
SCIENCE NEWS**
www.advancedsciencenews.com

**ADVANCED
OPTICAL
MATERIALS**
www.advopticalmat.de

Figure 1. Colloidal 2D MAPbBr$_3$ perovskites exhibit a distinct thickness with specific spectral features. a – d) TEM images of four samples with bulk-like and/or multi-layered nanosheets, exhibiting either rectangular or irregular lateral shapes, with the sample in d) being considerably smaller than the other samples and showing the characteristic optical properties. e) Nanosheets absorb and emit at specific spectral positions, which we assign to precise layer numbers, summarized in Table 1. f) Individual nanosheets contain different layer numbers at the same time, allowing for the transfer of energy and electrons.

corresponding PL features at 2.72, 2.62, and 2.36 eV (main peak). Individual nanosheets have a stacked structure containing multiple layer thicknesses, as is schematically shown in Figure 1f. Strong evidence for this stacked and mixed-n structure is discussed below. The sample which exclusively contains bulk-like MAPbBr$_3$ nanosheets (black), shows a single absorbance maximum at 2.38 eV and one PL maximum at 2.35 eV. Spectral features and respective layer numbers of all samples are summarized in **Table 1**. The PLQY of colloidal bulk MAPbBr$_3$ lies below 1% and increases significantly when other layer thicknesses are present. For example, the PLQY value rises to 31% when fractions with $n = 5, 7, 8$, and 10 are co-synthesized. Generally, thinner nanosheets exhibit reduced PLQY, but in our case, a lower n-value is not necessarily associated with thinner structures because of the stacked build-up of the nanosheets. Since the PL spectra mainly emit from the bulk region or other high-n fractions (as is shown in Figure 1f), the increased PLQY cannot be caused by higher PLQY from low-n fractions. Instead, we attribute this effect to transport processes from thinner to thicker layers, which will be discussed in the following.
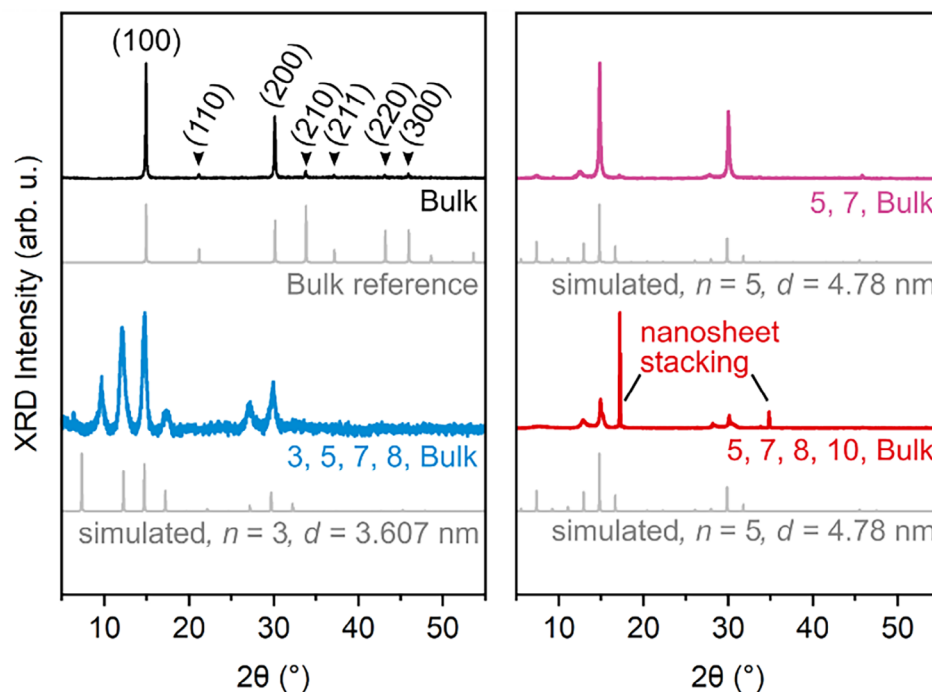
The assignment of n for the samples discussed here is supported by powder XRD data (see **Figure 2**). The bulk pattern is based on the crystallographic data of Elbaz et al.,[34] confirming the cubic crystal structure (Pm$\bar{3}$m). Simulated patterns in grey are obtained according to the method described by Klein et al.[4] Colloidal layered perovskite nano- and micro-crystals show periodic, nearly equidistant XRD intensity patterns plotted versus 2θ in the diffractograms. The position of the reflexes can provide information on the magnitude of the preferential orientation (texture effect) and stacking periodicity. Additionally, the relative intensity of the reflexes yields information on the number of monolayers and thus the organic spacer thickness. We find the best match to the experimental data is provided by n values of 3,

Table 1. Maxima and shoulders in absorption and PL spectra as well as PLQY of colloidal 2D MAPbBr$_3$ perovskites with different composition of layer numbers.

Sample ($n =$)		Spectral features (eV [nm])	PLQY
Bulk		2.38 [521]	0.2%
	Absorbance	2.38 [521]	
	PL	2.35 [528]	
3, 5, 7, 8, Bulk		2.88, 2.75, 2.64, —, 2.42 [430, 451, 470, —, 512]	3.6%
	Absorbance	2.88, 2.75, 2.64, —, 2.42 [430, 451, 470, —, 512]	
	PL	2.84, 2.72, 2.63, 2.57, 2.38 [437, 456, 471, 482, 521]	
5, 7, Bulk		2.76, 2.64, 2.38 [449, 470, 521]	14.3%
	Absorbance	2.76, 2.64, 2.38 [449, 470, 521]	
	PL	2.72, 2.62, 2.36 [456, 473, 525]	
5, 7, 8, 10, Bulk		2.77, 2.64, 2.55, 2.46[a], 2.33 [448, 470, 486, 504, 532]	31%
	Absorbance	2.77, 2.64, 2.55, 2.46[a], 2.33 [448, 470, 486, 504, 532]	
	PL	2.73, 2.61, 2.55[b], 2.45, 2.31[b] [454, 475. 486, 506, 537]	

[a] Corresponding ground state bleach in TAS measurements; [b] Determined with the second derivative of the PL spectrum.

5, and 5, for the three multi-layered samples, resp. and an organic spacer thickness of ≈18 Å, which correlates well with the length of the dodecylamine spacer (≈16.5 Å) and implies an intercalated ligand double layer. The n found by XRD analysis corresponds to the lowest n values in the respective sample evidenced by steady-state absorption and TAS. The higher-n pattern from the mixed

**ADVANCED
SCIENCE NEWS**

www.advancedsciencenews.com

**ADVANCED
OPTICAL
MATERIALS**

www.advopticalmat.de

Figure 2. Powder XRD patterns of all samples in comparison to calculated diffractograms in grey. Black: The bulk sample has a (100) orientation and a respective texture effect (enhancement of (h00) reflexes). (110), (210), (211) etc. are recognized. Blue: Layered nanosheets with n = 3, 5, 7, 8, and bulk, show a dominant n = 3 fraction. Pink: n = 5, 7, and bulk, with simulation showing a dominant n = 5 fraction. Red: n = 5, 7, 8, 10, and bulk, with simulation showing a dominant n = 5 fraction. Reflexes at 17.2° and 34.8° are caused by the stacking of the nanosheets, which is confirmed by TEM images (see Figure S2, Supporting Information).
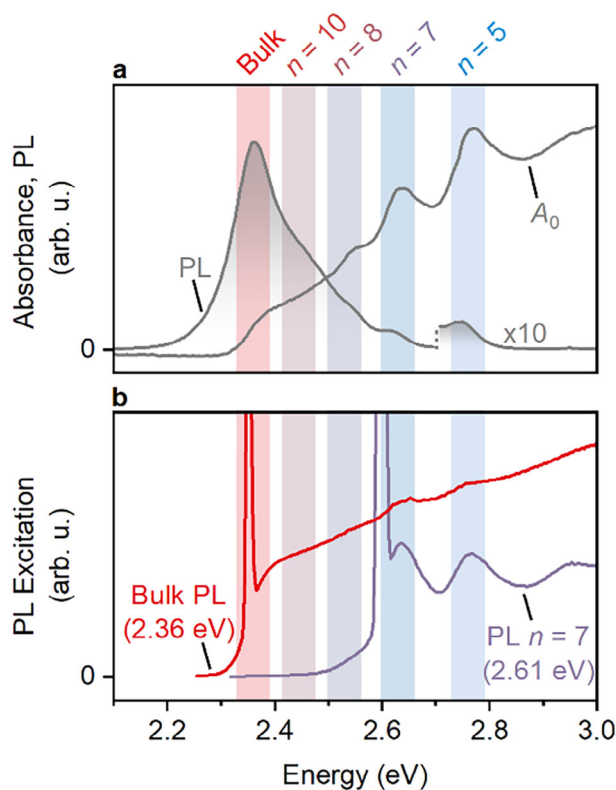
samples could not be clearly recognized due to their low intensity. In the "red" sample (5-7-8-10-bulk), very sharp reflexes at 17° and 34° 2θ were detected (Figure 2). These reflexes represent evidence for thick structures in the sample (up to 90 nm according to the Scherrer equation) and are attributed to the stacking of the layered nanosheets into thicker superstacks. An example of such a superstack is shown in Figure S2 (Supporting Information), confirming a superstack height of 70 to 120 nm. In the bulk sample, reflexes at 14.9°, 21.2°, 30.1°, 33.8°, 37.1°, 43.2°, 45.9° and 62.7° 2θ correspond well with the crystallographic planes (100), (110), (200), (210), (211), (220), (300), and (400).

Central to the investigation of transport processes in multi-layered MAPbBr$_3$ nanosheets is whether different layer numbers only occur in separate stacks or if they also coexist within the same perovskite nanosheet, as is schematically shown for n = 3 and 10 in Figure 1f. The scheme also shows an expected defect rich domain at the n-n interface inherent to multi-n RPPs, since adjacent layers are shifted by half a unit cell in RPPs.[35] The consequences of this defect-rich domain will be discussed later. The fact that we cannot separate layers by cascade centrifugation gives a first indication that individual nanosheets can contain more than one n. We back up this assumption by spectroscopic data, shown in **Figure 3**. For a sample containing n = 5, 7, 8, 10 and bulk nanosheets (see Figure 3a), the PL intensity of the bulk PL and the PL for n = 7, when changing the excitation energy is shown (see Figure 3b). For the bulk PL (red curve) in Figure 3b we find excitation features for n = 5, 7, and 8. The presence of these features suggests that excitation of thin-

ner MAPbBr$_3$ regions leads to emission from thicker layers in the same nanosheet, which means that energy or charge transfer must take place by crystal-crystal contacts. When following the PL of n = 7 (violet curve) for changing excitation energy, excitation features representing the absorbance for n = 5 and 7 get apparent. The crystal-crystal contact of the fractions n = 5 and n = 7 is also evident from this observation. Another argument supporting inter-region contacts is provided by TCSPC PL measurements, shown in Figure S3 (Supporting Information). PL signals from 2.34 eV to 2.76 eV, show that PL lifetimes get shorter with a decreasing layer number of the nanosheets. The bulk fraction shows longer-lived PL, which indicates that high-n regions in the nanosheets are populated via low-n regions by funneling processes, again indicating close crystal-crystal contact.

2.2. Excitons and Charge Carriers Recombine via Emission and Non-Radiative Auger Processes

To gain information about the underlying recombination processes in photoexcited MAPbBr$_3$ nanosheets, part of their steady-state absorbance spectra is modeled based on the Elliott theory.[30] The model is derived from studies by Yang et al., Chang et al., and Sestu et al.[31,36,37] and described in detail in the SI. The A_0 fitting procedure is performed for the energetically lowest transition associated with the highest layer number (bulk). The absorption data and the corresponding model are shown in **Figure 4a** for the bulk transition of MAPbBr$_3$, also containing bulk, 5- and

**ADVANCED
SCIENCE NEWS**

www.advancedsciencenews.com

**ADVANCED
OPTICAL
MATERIALS**

www.advopticalmat.de

Figure 3. Spectroscopic evidence for intercrystal contact in perovskite nanosheets with different layer numbers (for a sample containing n = 5, 7, 8, 10 and bulk nanosheets) in the same perovskite. a) Absorption (A_0) and PL spectrum with features caused by different layer numbers. The main features are marked by colored vertical bars. b) PL signal associated with bulk and n = 7 when changing the excitation energy (red and violet, resp.). Both PLE signals show features also present in the absorption spectrum above, which indicates the funneling of excited carriers into regions of higher layer numbers.

7-layered regions. The bulk absorption feature contains a charge carrier (green, A_{CC}) and an excitonic contribution (orange, A_{Exc}). The carrier contribution reflects all transitions of valence band electrons when excited into the conduction band (fundamental absorption), as shown in Figure 4b. The exciton contribution consists of discrete energy states of the bound electron-hole pair, as shown in Figure 4c, representing the exciton as a quasi-particle. In materials with low exciton binding energy such as high-n perovskite nanosheets, the excitonic 1s state is populated almost exclusively rather than energetically higher excited states. Up to the absorption shoulder of n = 7, the Elliott model accurately represents the absorption profile of multi-layered MAPbBr$_3$ perovskites nanosheets. We extract an exciton binding energy of 20 ± 8 meV and a bandgap of 2.38 ± 0.01 eV attributed to the bulk region. The E_b is less than $k_B T$ = 26 meV for 300 K, leading to dissociation of excitons in the bulk. The energetically higher transitions (associated with n = 5 and 7, resp.) are clearly visible in the absorption of the sample. These transitions mask A_{CC}(bulk) and render its shape for E > 2.6 eV speculative. Fitting the energetically higher absorption data to the Elliott model provides an estimate of the exciton binding energy of 136 meV for n = 5 (for details see Figure S5, Supporting Information). Based on $E_b(n$ =

5) > $k_B T$ > E_b(bulk), we can assume that the decay of excitons in low-n regions is significantly longer than in bulk regions at room temperature. A strong rise of E_b by thickness confinement is in excellent agreement with the literature on MAPbBr$_3$ and other perovskites.[38,39]

Figure 5a shows the transient changes in absorption when MAPbBr$_3$ perovskite nanosheets are photoexcited with short laser pulses (< 150 fs) and characterized by TAS. Here, a MAPbBr$_3$ RPP sample containing bulk, 5- and 7-layered fractions was photoexcited with an energy of 2.76 eV and a photon fluence of 50 µJ cm^{-2}. Multi-layered 2D perovskites were measured under constant stirring, which prevents photocharging[40] and yields orientation averaging of their anisotropic optical properties.[41] We probe a negative ΔA signal at 2.35 eV and a positive signal at 2.45 eV, both decaying over hundreds of picoseconds. The observed transient response is a reported pattern for MAPbBr$_3$ perovskites caused by three factors: (i) band filling, thus fading of the carrier band, (ii) bandgap renormalization (BGR), which causes a shift of the carrier band, and (iii) the presence of free charge carriers, which quench and broaden the excitonic absorption.[36] In Figure 5b, the fitting of an extended Elliott model (adapted from Chang et al.[31] and Yang et al.)[36] is shown (see detailed description in the SI) with excellent agreement with the measured data. In brief, we calculate the excited state absorption with $A^* = A_0 + s_{\Delta A}\Delta A$, with $s_{\Delta A}$ = 10 being an empirical scaling factor (further discussed in the SI). The fitting procedure yields time-dependent properties of the electronic structure: the bandgap E_g, the exciton binding energy E_b, the exciton bandwidth Γ, the quasi-Fermi energy E_{fq}, the carrier temperature T_e, and scaling factors f_1 and f_2, which are proportional to the oscillator strength of the free charge carrier and excitonic transitions, resp. The extended Elliott theory accurately represents the measured ΔA signal and hence serves as a basis for the evaluation of the decay processes in the multi-layered MAPbBr$_3$ perovskite nanosheets studied here.

For an intuitive interpretation of how the free charge carriers recombine, the extracted time-dependent properties are translated into a density of occupied states (DOS) for pump-probe delays of 10, 1000, and 5000 ps in Figure 5c. We find that 10 ps after photoexcitation, most of the free charge carriers in the conduction band exhibit an energy of 2.43 eV. After 1000 ps, both the area of the DOS and the bandgap decrease toward the relaxed system. Here, the area corresponds to the number of excited electrons N_e and is calculated from E_g and E_{fq} in the SI. Figure 5d shows that N_e as expected vanishes over time, which is induced by different decay processes: In our experimental set-up, the IRF of this measurement is ≈150 fs, which means that the excited charge carriers start to thermalize and equilibrate with the lattice temperature during photoexcitation.[42] Which recombination processes occur afterward mainly depends on N_e but also on the sample properties such as the defect concentration in multi-layered MAPbBr$_3$ perovskite nanosheets.[43] In general, higher N_e favors multi-particle recombination. The number of participating charge carriers in turn determines the order of the kinetic rate law by which N_e decays. Figure 5d shows the fits to the rate laws of order 1, 2, and 3 (light to dark green), underpinning that N_e of free charge, carriers is only poorly represented by first-order kinetics. This observation is expected since monomolecular recombination processes in perovskites only dominate at comparatively low charge carrier densities of
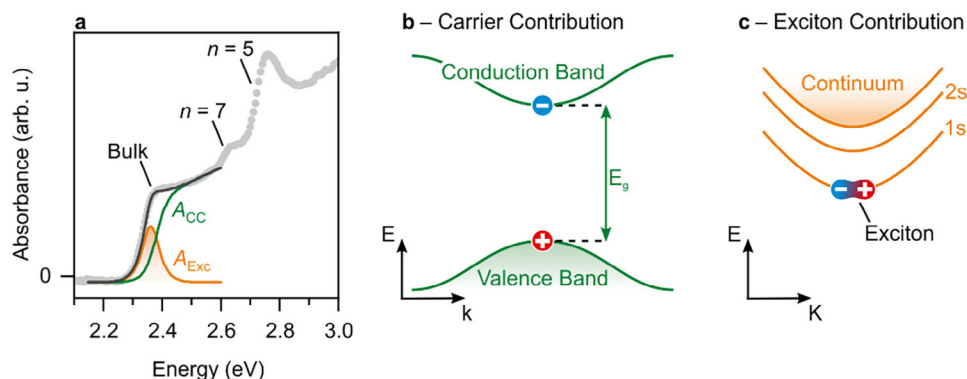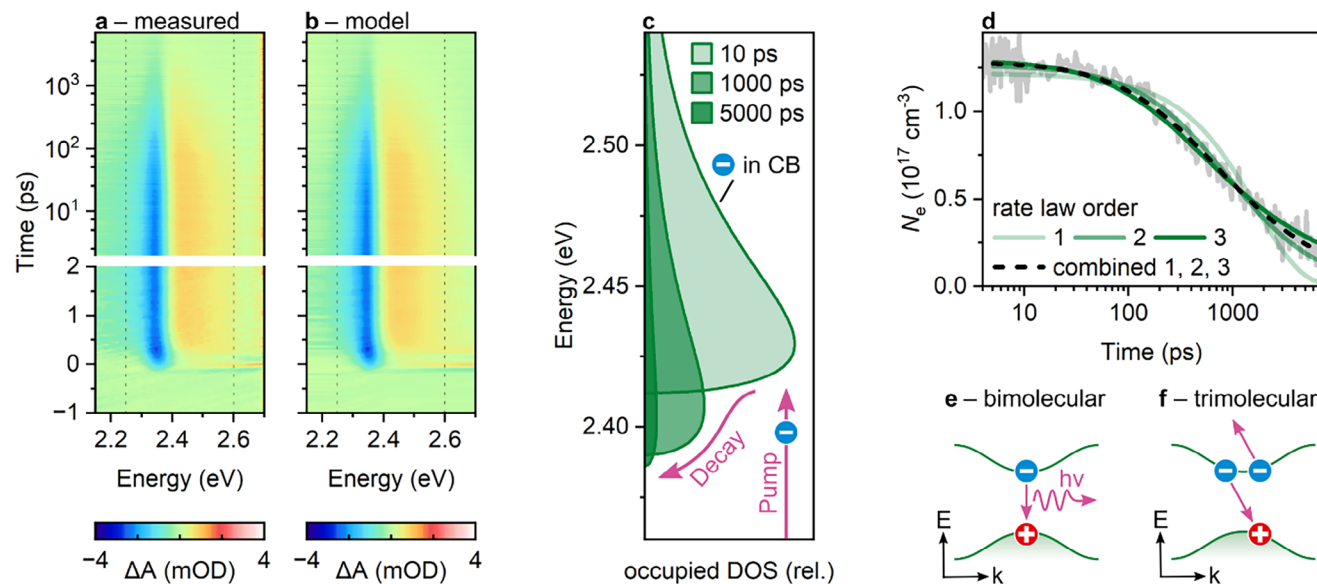
Figure 4. Colloidal MAPbBr$_3$ perovskite nanosheet absorption is based on charge carrier and exciton contributions. a) The absorption of MAPbBr$_3$ (n = 5, 7, and bulk) shows distinct features, which we assign to the regions of the respective layer numbers. Each absorption feature is composed of a step-like charge carrier contribution and a peak-like exciton contribution. b) The charge carrier contribution originates from the band structure. c) The exciton contribution reflects the binding states of the excited electron-hole pairs.
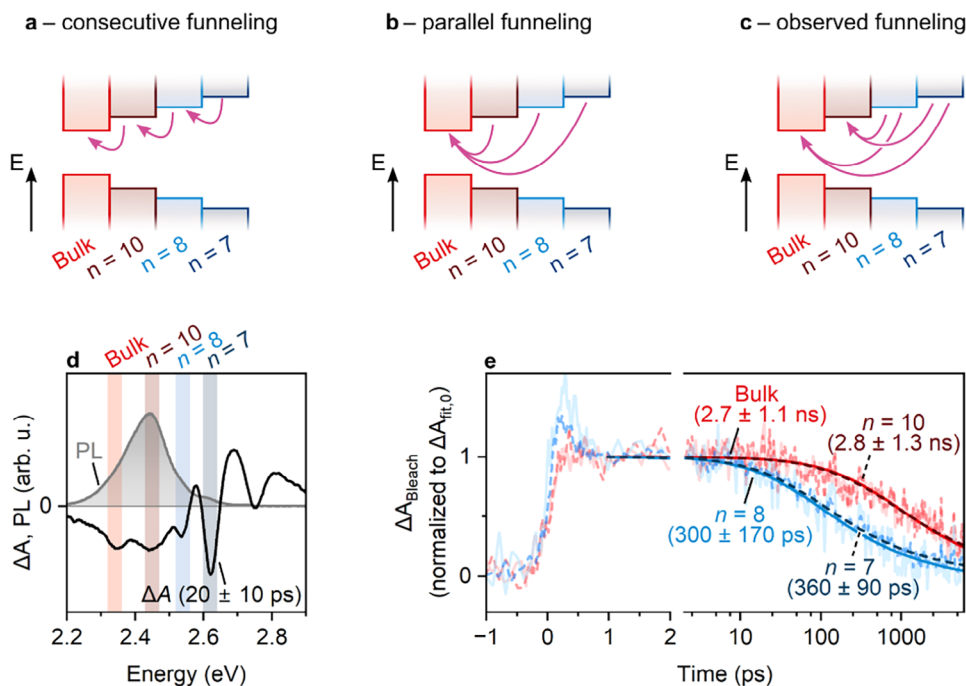
under 10^{15} cm^{-3}, which is three orders of magnitude below the fluences applied here.[44] Rate laws of second and third order, on the other hand, better follow the measured data. Second-order kinetics indicates the recombination of free electrons and holes or EEA, while a third order kinetic suggests three-body Auger recombination, as is schematically illustrated in Figures 5e and 4f. The determination of rate constants of the respective orders (k_1, k_2, and k_3) is shown as a dashed line in Figure 5d and calculated using the combined rate law (details given in the SI):

$$\frac{\partial N_e}{\partial t} = -k_1 \cdot N_e - k_2 \cdot N_e^2 - k_3 \cdot N_e^3 \qquad (1)$$

Fitting yields rate constants of k_1 = 1.5 · 10^{-8} ps^{-1}, k_2 = 1.2 · 10^{-21} cm^3/ps, and k_3 = 1.6 · 10^{-39} cm^6/ps and respective lifetimes of τ_1 = 65 µs, τ_2 = 2.5 ns, and τ_3 = 4.4 ns for $N_{e,0}$ = 1.16 · 10^{18} cm^{-3}. Again, the first order time constant τ_1 being in the microsecond range suggests that monomolecular processes are highly unlikely to occur. In contrast, both τ_2 and τ_3 are in the nanosecond range at this photoexcitation density. Therefore, both Auger and recombination of free charge carriers seem to occur with a rather similar probability. This assumption is supported by the PLQY = 14% not being quenched by Auger recombination. The relatively slow Auger recombination with respect to spherical nanocrystals was found in CsPbBr$_3$ perovskites as well and is caused by lower collision frequency of charge carriers

Figure 5. Excited charge carriers in MAPbBr$_3$ perovskite nanosheets relax via bi- and trimolecular processes. a) Measured transient ΔA map of MAPbBr$_3$ (n = 5, 7, and bulk) after photoexcitation at 2.76 eV, 50 µJ cm^{-2}, and b) corresponding modeled ΔA signal exhibiting excellent agreement (vertical lines are fitting limits). c) The density of populated states in the conduction band (CB) according to the Elliott model shows that charge carriers are quasi-Fermi distributed and gradually leave the conduction band. d) The total concentration of excited electrons N_e in the conduction band (grey) is fitted to first, second, and third order kinetics (light to dark green) and to a mixed order kinetic (dashed). N_e is dominated by a second and third order decay indicating bi- and trimolecular processes, schematically depicted in e) and f).

**ADVANCED
SCIENCE NEWS**

www.advancedsciencenews.com

**ADVANCED
OPTICAL
MATERIALS**

www.advopticalmat.de

Figure 6. Excited charge carriers in MAPbBr$_3$ perovskite nanosheets can funnel via alternative routes into thicker crystal domains. a–c) Schematic band structure of regimes with different layer numbers shows how excited electrons funnel on consecutive or parallel pathways, as well as the observed mixed funneling behavior. d) Spectral positions of $n = 5, 7, 8, 10$, and bulk are determined by steady-state PL (grey) and TAS (black, averaged from 10 to 30 ps), with the sample photoexcited at 3.10 eV at a low fluence of 6 μJ cm^{-2}. e) Time-resolved amplitudes of the bleach signals in d show that carriers from thinner layer number regions (light and dark blue) funnel into regions of higher thickness (light and dark red). Displayed decay times (in brackets) were calculated by fitting to mixed-order decay kinetics.

and a reduced Auger recombination probability per collision.[45] Since the majority of the excited charge carriers are retained for hundreds of picoseconds, we can investigate multi-n nanosheets regarding transport processes of both free charge carriers and excitons, which is described in detail in the following section.

2.3. Funneling and Exciton Self-Trapping Compete on Picosecond Timescales

To study the role of funneling in multi-n perovskite nanosheets, we examine RPPs that respond with multiple signals to photoexcitation. In principle, there are two edge cases for the sequencing in which funneling might take place: (i) Consecutively, by charge carriers and excitons moving in a strictly ascending order through different layer numbers, schematically shown in **Figure 6a**. In this case, longer decays of the transient responses of higher n should be observed when all n are excited simultaneously. (ii) Parallel funneling channels exist from all n to the most energetically favored state, i.e., to the thickest layer n shown in Figure 6b. Transient signals of the thickest nanosheet fraction are expected to exhibit the longest decay times. All other signals should show shorter decays which are similar to one another, if funneling is the fastest decay process. However, we find a mixed form of the described paths occurring, as illustrated in Figure 6c (more detail below). Figure 6d shows the PL (grey) of a sample that contains layer numbers of $n = 5, 7, 8, 10$, and bulk. The sample has the highest PL intensity at 2.45 eV, which means it does

not emit preferentially from the layer number with the smallest bandgap. This indicates that funneling from $n = 10$ to bulk is slow in this sample.

When photoexciting charge carriers of all n simultaneously (at 3.10 eV with 6 μJ cm^{-2}), responses of all layer numbers are visible as negative signals in the ΔA spectrum (black, averaged from 10 to 30 ps). Additional spectral linecuts of this measurement are shown in Figure S9 (Supporting Information). Since we can assign a layer number to each bleach signal, their transients provide information on how excited charge carriers and excitons funnel between different n. The normalized ΔA decays of the different layer numbers are shown in Figure 6e and fitted with rate laws of mixed order (first, second, third). The $1/e$ lifetimes are then determined from the fitted decay curves (for mathematical details see SI). Interestingly, we find two fast and two slow decays. The bleach signals of $n = 10$ and bulk decay with similar constants of 2.8 ± 1.3 ns and 2.7 ± 1.1 ns, resp., whereas the signals of $n = 7$ and 8 exhibit shorter similar constants of of 360 ± 90 ps and 300 ± 170 ps, resp. These decays confirm that funneling takes place indeed in an ascending layer number direction. Since $\tau (n = 10) \approx \tau$(bulk) we conclude that almost no charge carriers funnel from $n = 10$ regimes into the bulk fraction in this sample. This assumption is additionally confirmed by the sample PL centered at 2.45 eV, i.e., the energy associated with $n = 10$. Typically, time constants of charge carrier transfer in perovskites are reported to lie in the picosecond to nanosecond range,[46] which is considerably slower than energy transfer like Förster resonance energy transfer (FRET) taking place in less than a picosecond.[47]
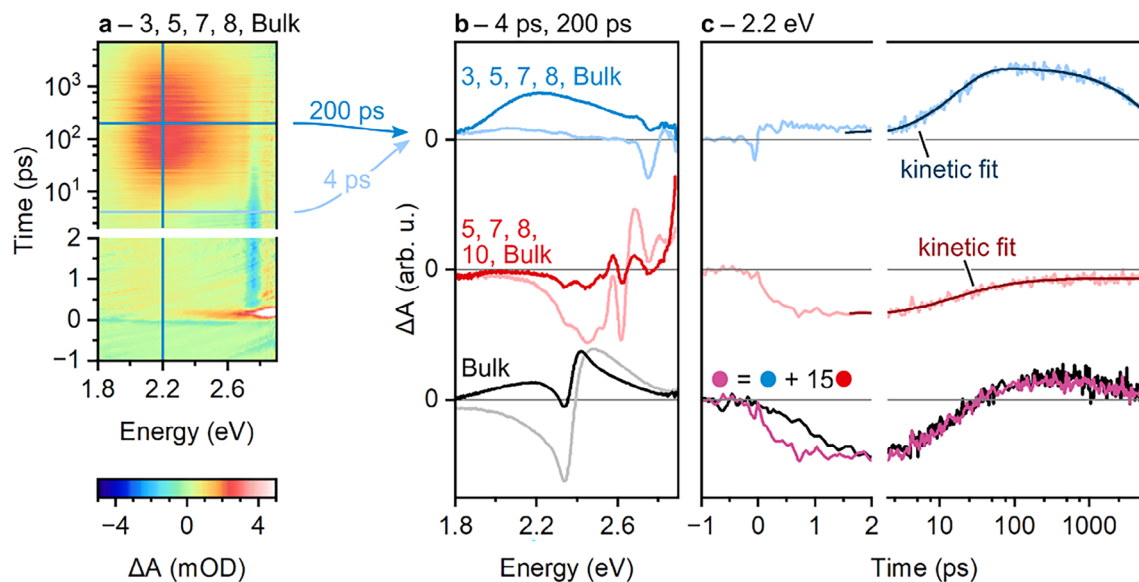
Figure 7. Excitons might be trapped during funneling. a) ΔA map of an MAPbBr$_3$ RPP nanosheet sample containing n = 3, 5, 7, 8, and bulk, photoexcited at 3.41 eV with 50 μJ cm^{-2}. Besides the bleach signal at 2.75 eV, a broad PIA appears 10 ps after excitation. b) ΔA spectral linecuts at 4.0 ± 0.4 ps and 200 ± 20 ps (light and dark blue) and linecuts at the same times for a sample containing n = 5, 7, 8, 10, and bulk (red, pump: 3.1 eV, 50 μJ cm^{-2}), and a sample of bulk only (black, pump: 3.41 eV, 50 μJ cm^{-2}). c) Corresponding ΔA traces at 2.2 eV ± 20 meV with kinetic fits and the mirroring of the response of the bulk perovskite by combining the other two measurements shows that exciton trapping and gain might be competing processes in multi-n MAPbBr$_3$ RPP nanosheets.

With our measured decay times in the picosecond and nanosecond range, we assume that charge carriers are transferred rather than energy.

If mixed-n MAPbBr$_3$ perovskite nanosheets are excited with higher fluences (≥50 μJ/cm^2), additional interesting photophysics occur, which helps to investigate ultrafast charge carrier processes. **Figure 7a** shows a photoinduced absorption (PIA) appearing at 2.2 eV for a colloidal MAPbBr$_3$ nanosheet sample with n = 3, 5, 7, 8, and bulk, which is photoexcited at 3.41 eV. The PIA signal has a rather broad width of 1 eV (see Figure 7b) and, in contrast to the bleach signal at 2.65 eV, cannot be explained via the Elliott model. We infer that effects that modify the exciton line shape or change the shape and occupation of the bands are not responsible for the observed PIA. Due to the broad nature of the signal, we assume exciton self-trapping at nonspecific energies, e.g. at edges or defects in the nanosheets. Localized excitons have been suspected in CsPbBr$_3$ and mixed Ag–Sb/Bi perovskites before,[48,49] however to the best of our knowledge, time-resolved studies on trapped excitons in MAPbBr$_3$ perovskites have not been described yet. Lin et al. observed a broad PIA for bromide-rich naphthalene diammonium perovskites with n = 1 and attributed the feature to a naphthalene triplet species.[50] As opposed to these perovskites, the PIA in the MAPbBr$_3$ nanosheet samples shown here rises over tens of picoseconds, as is shown by the progression of ΔA at 2.2 eV ± 20 meV in Figure 7c. The PIA follows the kinetic scheme of two consecutive elementary steps (PIA growing and decaying) as depicted by the fit curve (dark blue). The analytical solution to this scheme can be presented as

$$\Delta A_{PIA}(t) = c \cdot \frac{\tau_{grow}}{\tau_{grow} - \tau_{decay}} \cdot \left(e^{-t/\tau_{grow}} - e^{-t/\tau_{decay}} \right) \quad (2)$$

and yields constants of τ_{grow} = 16.2 ± 0.3 ps, and τ_{decay} = 5.97 ± 0.12 ns. ΔA_{PIA} is the time-dependent change of the absorption when excited, and c is a scaling factor. The fact that the ΔA of the PIA is accurately represented by the described rate law indicates monomolecular processes for both, the growth and the decay step. Accordingly, a plausible explanation for this constant τ_{grow} and spontaneous relaxation with τ_{decay} is the self-trapping of excitons/charge carriers and their subsequent recombination.

In comparison, for a sample with n = 5, 7, 8, 10, and bulk, photoexcitation does not lead to the broad PIA described above, as is illustrated by the spectral cuts and transients in red in Figure 7b,c. Spectral linecuts at additional pump probe delays are shown in Figure S10 (Supporting Information). The sample is photoexcited with a fluence of 50 μJ cm^{-2} at an energy of 3.1 eV, generating excitons and free charge carriers in each layer number, which is supported by the respective narrow bleach signals. The absence of a broad PIA signal implies that excitons are not trapped in this sample. Instead, a negative ΔA signal is observed, which can be caused by gain, decays with τ = 27.7 ± 2.6 ps by a second order kinetic scheme and is broadened with respect to the measured PL. A high PLQY of 14% compared to the RPP sample with 3.6% (n = 3, 5, 7, 8, and bulk) also indicates that excitons are substantially less trapped and then recombine non-radiatively in samples with a better n-n connectivity. The crystalline quality and surface passivation of multi-layered MAPbBr$_3$ perovskite nanosheets play a crucial role in efficient PL since a high number of free electrons is needed for optical gain, as has been shown for MAPbI$_3$ perovskites.[51] Consequently, both, the broad PIA and gain, can be observed in parallel when stimulated emission occurs before charge carriers are trapped in localized states. In Figure 7b,c in black, this observation is made on MAPbBr$_3$ perovskites, which contain bulk-like layer numbers only. The temporal evolution of

ΔA can be recreated as a linear combination of the two cases, where either a broad PIA or gain is present (pink in Figure 7c). This gives solid evidence that multiple factors, such as the combination of n, defect density, and the n-n connectivity have influence on whether exciton-trapping or gain is dominating in the colloidal samples.

3. Conclusion

In this work we have addressed recombination (pathways) and funneling processes in colloidal multi-layered 2D MAPbBr$_3$ perovskite nanosheets. By applying an extended Elliott model we find that after photoexcitation with a fluence ≤ 50 µJ/cm^2, second and third order processes dominate recombination in the nanosheets. Funneling in MAPbBr$_3$ nanosheets can occur when thinner layer numbers are connected with higher-n layers. Long lived low-n excitons ($E_b > 100$ meV) funnel into high-n layers with $\tau = 10$ to 50 ps, where their E_b is drastically decreased below $k_B T = 26$ meV at room temperature. Depending on the connectivity of the layers with different n, the excitons and charge carriers funnel into the direction of increasing thickness, but can accumulate in intermediate n, where they recombine radiatively or by Auger processes. Additionally, we found evidence that the quality of the n-n interface determines whether exciton trapping occurs and thus competes with funneling. This study shows that funneling and self-trapping processes in RPPs could be key parameters for designing energetic pathways for excitons and free charge carriers for future efficient RPP-based devices.

The structure, quality, and size of n-n interfaces define the kinetics of trapping processes in mixed-n perovskite nanosheets and are subject to further synthetic improvement. Funneling in the nanosheets exhibits mixed characters (consecutive and parallel) and allows for different charge transfer and transport configurations. When comparing mixed-n nanosheets with their bulk-like counterparts, we envision application possibilities for the nanosheets toward directional funneling and exciton binding energy downscaling, which could help to outcompete trapping and EEA.

4. Experimental Section

Steady-State Spectroscopy: UV/vis absorption spectra were obtained with a Lambda 1050+ spectrophotometer from Perkin Elmer equipped with an integration-sphere. The PL measurements were performed with a fluorescence spectrometer (Spectrofluorometer FS5, Edinburgh Instruments). PLQYs of the samples were determined using an absolute method by directly exciting the sample solution and the reference (toluene in our case) in an SC-30 integrating sphere module fitted to the Spectrofluorometer FS5 from Edinburgh Instruments. During the measurement, the excitation slit was set to 6.5 nm, and the emission slit was adjusted to obtain a signal level of 10^6 cps, the excitation wavelength was chosen at 375 nm with 50 µW cm^{-2} irradiance. A wavelength step size of 0.1 nm and an integration time of 0.2 s was used. The calculation of absolute PLQY was based on the formula, $\eta = \frac{E_{sample} - E_{ref}}{S_{ref} - S_{sample}}$, where η was the absolute PLQY, E_{sample} and E_{ref} were the integrals at the emission region for the sample and the reference, resp., and S_{sample} and S_{ref} were the integrals at the excitation scatter region for the sample and the reference, respectively. The selection and calculation of integrals from the emission and excitation scattering region and the calculation of absolute PLQY were performed using the FLUORACLE software from the Edinburgh Instruments.

Transient Absorption Spectroscopy (TAS):   Ultrafast carrier dynamics of colloidal MAPbBr$_3$ perovskite nanosheets were studied by femtosecond transient absorption spectroscopy. The samples were dispersed in toluene under inert gas conditions and measured inside a 2 mm quartz glass cuvette with constant stirring. Laser pulses (120 fs, 1.54 eV or 90 fs, 1.55 eV) with a repetition rate of 1 kHz were generated by a Ti:sapphire regenerative amplifier system (Astrella-F from Coherent or Spitfire ACE from Spectra-Physics) and split 90:10 into pump and probe pulses. The pump beam was led into an optical parametric amplifier and second harmonics generation system (Appollo-T by Ultrafast Systems or TOPAS Prime by Spectra-Physics), where its energy was adjusted by nonlinear frequency mixing to the desired excitation energy between 0.77 and 4.28 eV. The probe pulse was transformed into a broadband supercontinuum by nonlinear processes in a CaF$_2$ or sapphire crystal. Accordingly, probing takes place in an energy range from 1.55 to 3.87 eV. The overlap of pump and probe pulses within the sample was optimized before each measurement to achieve the best signal-to-noise ratio. The attenuated probe pulse was led into a fiber-coupled spectrometer (Ultrafast, Helios Fire) with a linear detector array. The charge carrier dynamics via the absorption changes were studied by varying the delay times between probe and pump pulse. The pump-probe delay was electronically controlled with a delay line and covers a time window of up to 8 ns after photoexcitation.

Transmission Electron Microscopy (TEM):   TEM samples were prepared by diluting the nanosheet suspension with toluene followed by drop casting 10 µL of the suspension on a TEM copper grid coated with a carbon film. Standard images were done on a Talos-L120C and EM-912 Omega with a thermal emitter operated at an acceleration voltage of 120 kV and 100 kV.

X-Ray Diffraction (XRD):   Measurements were performed on a Panalytical Aeris System with a Bragg-Brentano geometry and a copper anode with an X-ray wavelength of 0.154 nm from the Cu-kα1 line. The samples were measured by drop-casting the suspended samples on a $\langle 911 \rangle$ or $\langle 711 \rangle$ cut silicon substrate. Powder XRD patterns were simulated with the PowderCell package,[52] Version 2.4. The inorganic part of the crystal (Pb-Br) unit was used to simulate the pattern with Rietveld-Toraya (plate) preferred orientation in [001] direction based on the crystallographic information from Elbaz et al.[34] Unit cells were formed with different n from 2 to 6 in Ruddlesden-Popper stacking configuration.

Supporting Information

Supporting Information is available from the Wiley Online Library or from the author.

Conflict of Interest

The authors declare no conflict of interest.

Data Availability Statement

The data that support the findings of this study are available from the corresponding author upon reasonable request.

Keywords

[1] A. Martinez-Gracia, I. Arauzo, J. Uche, In *Solar Hydrogen Production* (Eds.: Calise, F., D'Accadia, M. D., Santarelli, M., Lanzini, A., Ferrero, D.), Academic Press, Amsterdam, Netherlands, **2019**.

[2] Best Research-Cell Efficiency Chart, **2024**, https://org.doi/www.nrel.gov/pv/cell-efficiency.html (accessed: March 2024).

[3] Y. Tong, F. Ehrat, W. Vanderlinden, C. Cardenas-Daw, J. K. Stolarczyk, L. Polavarapu, A. S. Urban, *ACS Nano* **2016**, *10*, 10936.

[4] E. Klein, A. Black, Ö. Tokmak, C. Strelow, R. Lesyuk, C. Klinke, *ACS Nano* **2019**, *13*, 6955.

[5] N. Mondal, A. De, A. Samanta, *ACS Energy Lett.* **2019**, *4*, 32.

[6] G. Rainò, N. Yazdani, S. C. Boehme, M. Kober-Czerny, C. Zhu, F. Krieg, M. D. Rossell, R. Erni, V. Wood, I. Infante, M. V. Kovalenko, *Nat. Commun.* **2022**, *13*, 2587.

[7] M. B. Fridriksson, S. Maheshwari, F. C. Grozema, *J. Phys. Chem. C* **2020**, *124*, 22096.

[8] N. Wang, L. Cheng, R. Ge, S. Zhang, Y. Miao, W. Zou, C. Yi, Y. Sun, Y. Cao, R. Yang, Y. Wei, Q. Guo, Y. Ke, Y. Mu, Y. Jin, Y. Liu, Q. Ding, D. Di, L. Yang, G. Xing, H. Tian, C. Jin, F. Gao, R. H. Friend, J. Wang, W. Huang, *Nat. Photonics* **2016**, *10*, 699.

[9] B.-H. Li, H. Di, H. Li, J.-C. Wang, W. Zeng, D.-B. Cheng, C. Zhou, X. Wang, Y. Shi, J. Song, Y. Zhao, X. Yang, Z. Ren, *J. Am. Chem. Soc.* **2024**, *146*, 6974.

[10] C. Liang, H. Gu, Y. Xia, Z. Wang, X. Liu, J. Xia, S. Zuo, Y. Hu, X. Gao, W. Hui, L. Chao, T. Niu, M. Fang, H. Lu, H. Dong, H. Yu, S. Chen, X. Ran, L. Song, B. Li, J. Zhang, Y. Peng, G. Shao, J. Wang, Y. Chen, G. Xing, W. Huang, *Nat. Energy* **2021**, *6*, 38.

[11] C. C. Stoumpos, D. H. Cao, D. J. Clark, J. Young, J. M. Rondinelli, J. I. Jang, J. T. Hupp, M. G. Kanatzidis, *Chem. Mater.* **2016**, *28*, 2852.

[12] P. Tyagi, S. M. Arveson, W. A. Tisdale, *J. Phys. Chem. Lett.* **2015**, *6*, 1911.

[13] Y.-H. Chang, J.-C. Lin, Y.-C. Chen, T.-R. Kuo, D.-Y. Wang, *Nanoscale Res. Lett.* **2018**, *13*, 247.

[14] B. J. Bohn, Y. Tong, M. Gramlich, M. L. Lai, M. Döblinger, K. Wang, R. L. Z. Hoye, P. Müller-Buschbaum, S. D. Stranks, A. S. Urban, L. Polavarapu, J. Feldmann, *Nano Lett.* **2018**, *18*, 5231.

[15] L. Kong, X. Zhang, Y. Li, H. Wang, Y. Jiang, S. Wang, M. You, C. Zhang, T. Zhang, S. V. Kershaw, W. Zheng, Y. Yang, Q. Lin, M. Yuan, A. L. Rogach, X. Yang, *Nat. Commun.* **2021**, *12*, 1246.

[16] L. Ma, M.-G. Ju, J. Dai, X. C. Zeng, *Nanoscale* **2018**, *10*, 11314.

[17] F. Yuan, G. Folpini, T. Liu, U. Singh, A. Treglia, J. W. M. Lim, J. Klarbring, S. I. Simak, I. A. Abrikosov, T. C. Sum, A. Petrozza, F. Gao, *Nat. Photonics* **2024**, *18*, 170.

[18] W. Zia, M. Malekshahi Byranvand, T. Rudolph, M. Rai, M. Kot, C. Das, M. Kedia, M. Zohdi, W. Zuo, V. Yeddu, M. I. Saidaminov, J. I. Flege, T. Kirchartz, M. Saliba, *ACS Energy Lett.* **2024**, *9*, 1017.

[19] J. Enomoto, R. Sato, M. Yokoyama, T. Kimura, N. Oshita, K. Umemoto, S. Asakura, A. Masuhara, *RSC Adv.* **2022**, *12*, 5571.

[20] J. Chen, J. Luo, E. Hou, P. Song, Y. Li, C. Sun, W. Feng, S. Cheng, H. Zhang, L. Xie, C. Tian, Z. Wei, *Nat. Photonics* **2024**, *18*, 464.

[21] L. Lanzetta, T. Webb, N. Zibouche, X. Liang, D. Ding, G. Min, R. J. E. Westbrook, B. Gaggio, T. J. Macdonald, M. S. Islam, S. A. Haque, *Nat. Commun.* **2021**, *12*, 2853.

[22] S. Caicedo-Dávila, P. Caprioglio, F. Lehmann, S. Levcenco, M. Stolterfoht, D. Neher, L. Kronik, D. Abou-Ras, *Adv. Funct. Mater.* **2023**, *33*, 2305240.

[23] C. Katan, N. Mercier, J. Even, *Chem. Rev.* **2019**, *119*, 3140.

[24] J.-C. Blancon, A. V. Stier, H. Tsai, W. Nie, C. C. Stoumpos, B. Traoré, L. Pedesseau, M. Kepenekian, F. Katsutani, G. T. Noe, J. Kono, S. Tretiak, S. A. Crooker, C. Katan, M. G. Kanatzidis, J. J. Crochet, J. Even, A. D. Mohite, *Nat. Commun.* **2018**, *9*, 2254.

[25] R. L. Milot, R. J. Sutton, G. E. Eperon, A. A. Haghighirad, J. Martinez Hardigree, L. Miranda, H. J. Snaith, M. B. Johnston, L. M. Herz, *Nano Lett.* **2016**, *16*, 7001.

[26] A. M. Oddo, M. Gao, D. Weinberg, J. Jin, M. C. Folgueras, C. Song, C. Ophus, T. Mani, E. Rabani, P. Yang, *Nano Lett.* **2023**, *23*, 11469.

[27] Y. Li, X. Luo, T. Ding, X. Lu, K. Wu, *Angew. Chem.* **2020**, *132*, 14398.

[28] V. I. Klimov, A. A. Mikhailovsky, S. Xu, A. Malko, J. A. Hollingsworth, C. A. Leatherdale, H.-J. Eisler, M. G. Bawendi, *Science* **2000**, *290*, 314.

[29] J. Lim, Y.-S. Park, K. Wu, H. J. Yun, V. I. Klimov, *Nano Lett.* **2018**, *18*, 6645.

[30] R. J. Elliott, *Phys. Rev.* **1957**, *108*, 1384.

[31] Q. Chang, D. Bao, B. Chen, H. Hu, X. Chen, H. Sun, Y. M. Lam, J.-X. Zhu, D. Zhao, E. E. M. Chia, *Commun. Phys.* **2022**, *5*, 1.

[32] M. Rahil, R. M. Ansari, S. Ahmad, S. S. Islam, *ACS Appl. Nano Mater.* **2023**, *6*, 5187.

[33] K. M. Forlano, C. R. Roy, W. Mihalyi-Koch, T. Hossain, K. Sanders, I. Guzei, K. R. Graham, J. C. Wright, S. Jin, *ACS Mater. Lett.* **2023**, *5*, 2913.

[34] G. A. Elbaz, D. B. Straus, O. E. Semonin, T. D. Hull, D. W. Paley, P. Kim, J. S. Owen, C. R. Kagan, X. Roy, *Nano Lett.* **2017**, *17*, 1727.

[35] L. Mao, C. C. Stoumpos, M. G. Kanatzidis, *J. Am. Chem. Soc.* **2019**, *141*, 1171.

[36] Y. Yang, D. P. Ostrowski, R. M. France, K. Zhu, J. van de Lagemaat, J. M. Luther, M. C. Beard, *Nat. Photonics* **2016**, *10*, 53.

[37] N. Sestu, M. Cadelano, V. Sarritzu, F. Chen, D. Marongiu, R. Piras, M. Mainas, F. Quochi, M. Saba, A. Mura, G. Bongiovanni, *J. Phys. Chem. Lett.* **2015**, *6*, 4566.

[38] K. Zheng, Q. Zhu, M. Abdellah, M. E. Messing, W. Zhang, A. Generalov, Y. Niu, L. Ribaud, S. E. Canton, T. Pullerits, *J. Phys. Chem. Lett.* **2015**, *6*, 2969.

[39] Q. Wang, X.-D. Liu, Y.-H. Qiu, K. Chen, L. Zhou, Q.-Q. Wang, *AIP Adv.* **2018**, *8*, 025108.

[40] F. Manteiga Vázquez, Q. Yu, L. F. Klepzig, L. D. A. Siebbeles, R. W. Crisp, J. Lauth, *J. Phys. Chem. Lett.* **2021**, *12*, 680.

[41] C. Ge, Y. Li, H. Song, Q. Xie, L. Zhang, X. Ma, J. Liu, X. Guo, Y. Yan, D. Liu, W. Zhang, S. Liu, Y. Liu, *Nat. Commun.* **2024**, *15*, 914.

[42] J. M. Richter, F. Branchi, F. Valduga de Almeida Camargo, B. Zhao, R. H. Friend, G. Cerullo, F. Deschler, *Nat. Commun.* **2017**, *8*, 376.

[43] T. C. Sum, N. Mathews, G. Xing, S. S. Lim, W. K. Chong, D. Giovanni, H. A. Dewi, *Acc. Chem. Res.* **2016**, *49*, 294.

[44] C. Wehrenfennig, G. E. Eperon, M. B. Johnston, H. J. Snaith, L. M. Herz, *Adv. Mater.* **2014**, *26*, 1584.

[45] Q. Li, Y. Yang, W. Que, T. Lian, *Nano Lett.* **2019**, *19*, 5620.

[46] Z. Gan, W. Chen, C. Zhou, L. Yu, L. Dong, B. Jia, X. Wen, *J. Phys. Chem. Lett.* **2020**, *11*, 5963.

[47] A. H. Proppe, M. H. Elkins, O. Voznyy, R. D. Pensack, F. Zapata, L. V. Besteiro, L. N. Quan, R. Quintero-Bermudez, P. Todorovic, S. O. Kelley, A. O. Govorov, S. K. Gray, I. Infante, E. H. Sargent, G. D. Scholes, *J. Phys. Chem. Lett.* **2019**, *10*, 419.

[48] A. Suhail, M. Bag, *ACS Appl. Nano Mater* **2023**, *6*, 16864.

[49] B. Yang, F. Hong, J. Chen, Y. Tang, L. Yang, Y. Sang, X. Xia, J. Guo, H. He, S. Yang, W. Deng, K. Han, *Angew. Chem.* **2019**, *131*, 2300.

[50] Y. L. Lin, J. C. Johnson, *J. Phys. Chem. Lett.* **2021**, *12*, 4793.

[51] B. R. Sutherland, S. Hoogland, M. M. Adachi, P. Kanjanaboos, C. T. O. Wong, J. J. McDowell, J. Xu, O. Voznyy, Z. Ning, A. J. Houtepen, E. H. Sargent, *Adv. Mater.* **2015**, *27*, 53.

[52] W. Kraus, G. Nolze, *J. Appl. Crystallogr.* **1996**, *29*, 301.